# Phase-field modeling for investigating the effect of rebar positioning and uniform versus non-uniform corrosion on concrete fracture

Ba-Thanh Vu, Xuan-Lam Nguyen*, Dac-Duc Nguyen, The-Truyen Tran, Duc-Nhiem Tran, Ngoc-Long Nguyen, Tien-Thanh Bui

*Faculty of Civil Engineering, University of Transport and Communications, Hanoi, Vietnam*

*thanhvb@utc.edu.vn, nxlam@utc.edu.vn, ngdacduc@utc.edu.vn, tranthetruyen@utc.edu.vn, tdnhiem@utc.edu.vn, nguyenngoclong@utc.edu.vn, btthanh@utc.edu.vn*

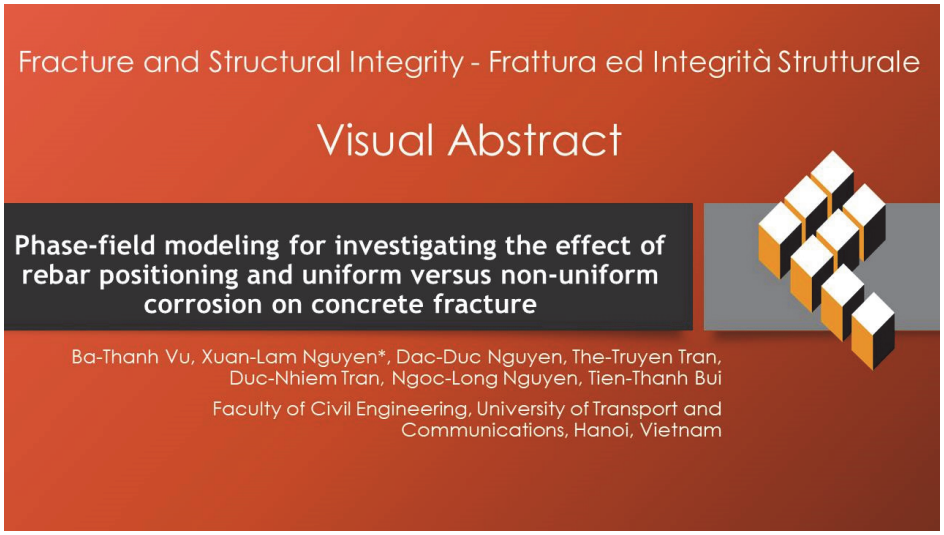


**Citation:** Vu, B.T., Nguyen, X.L., Nguyen, D.D., Tran, T.T., Tran, D.N., Nguyen, N.L., Bui, T.T., Phase-field modeling for investigating the effect of rebar positioning and uniform versus non-uniform corrosion on concrete fracture, Frattura ed Integrità Strutturale, 73 (2025) 166-180.

**Received:** 04.12.2024
**Accepted:** 20.05.2025
**Published:** 24.05.2028
**Issue:** 07.2025



**KEYWORDS.** Phase-field modeling, RC structures, uniform corrosion, non-uniform corrosion, crack, displacement of rust expansion.

## INTRODUCTION

The construction industry widely uses reinforced concrete (RC) structures due to their excellent technical properties and high durability. However, the RC structures are significantly affected by corrosion when exposed to environments containing high concentrations of chloride ions and/or carbon dioxide. This corrosion causes a reduction in bond strength and the delamination of the concrete cover due to the expansion volume of the rebar rust products, which are many times greater than the original volume of the rebars [1, 2]. Additionally, carbon dioxide, in combination with atmospheric humidity, can penetrate the micropores of the concrete, where it reacts with alkaline substances, resulting in the carbonation of the concrete, which also leads to concrete cracking [3].

Numerous studies have been conducted to assess damage in the RC structures and determine the level of rebar corrosion by using various methods. Experimental studies are commonly employed, with the accelerated corrosion test being the most widely used [4-6]. The goal of the accelerated corrosion test is to induce corrosion at a velocity much faster than would naturally occur. To optimize research time and ensure realistic corrosion levels, current densities are typically

recommended to range from 100 μA/cm² to 500 μA/cm² [5]. Tran et al., [6] used the accelerated corrosion test with a current density of 300 μA/cm² on the RC beams and obtained promising results. Furthermore, Qiao et al., [7] conducted experimental studies to investigate the impact of non-uniform and localized corrosion on crack propagation in concrete by immersing the RC specimens in a NaCl solution tank. Andrade et al., [8] also observed that even a very thin rust layer of corrosion on the rebar could lead to significant cracking in the RC structure. Additionally, the study [9] proposed the use of polypyrrole films applied to the rebar to protect against corrosion without compromising the bond properties between the concrete and rebar. These studies generally investigate corrosion along the rebar and assume either uniform or non-uniform corrosion to apply to the structural analysis programs.

Besides, several theoretical studies have been developed to predict the amount of corrosion and the time to crack initiation in the concrete cover. Bhargava et al., [10] proposed an analytical model to assess the fracture time of the concrete cover by considering the remaining strength of the cracked concrete layer, as well as the combined stiffness of the rebar and corrosion-induced rust products. Lu et al., [1] also developed a mathematical model to investigate the damage time based on the relationship between the radial pressure of corrosion products and the percentage of the rebar weight loss due to corrosion.

In recent decades, the high-performance computing systems have developed rapidly. Therefore, simulation methods have also advanced to study damage behavior due to corrosion, such as the Discrete Element Method (DEM) [11] and the Rigid-Body-Spring Method [12]. Pan and Lu [13] proposed the stochastic modeling of reinforced concrete cracking due to non-uniform corrosion based on the finite element method (FEM). Yang et al., [14] used the analytical model for non-uniform corrosion-induced concrete cracking based on the semi-elliptical assumption. The study [15] described the cracking of the concrete cover due to rebar corrosion by using the two-dimensional lattice model. Zhang et al., [16] developed the damage plasticity model to investigate the concrete cover crack propagation due to elliptical non-uniform corrosion of rebar. Du et al., [17] provided the interfacial transition zone model to simulate the damage due to rebar corrosion in the structures containing multiphase by considering the interfacial effect between matrix and aggregate. Recently, the phase-field method has emerged as a reliable numerical method to predict the structural fracture in various materials or under different loading conditions, including brittle/quasi-brittle materials [18-20], ductile materials [21], and dynamic crack development [22]. However, the studies [18-22] did not satisfy the strain orthogonal conditions as proposed in the theory of He and Shao [23]. This orthogonal condition combined with the phase-field method, helps improve the accuracy of the material response after structural damage occurs. This has been corroborated in the studies, where the phase-field method was integrated with strain orthogonal conditions [23] to simulate the homogeneous materials [24], the anisotropic materials [25], the damage considering interface effects between the phases [26], and the optimization of the matrix-inclusion structures [27].

Furthermore, in the previous studies on corrosion problems, the phase-field method has typically considered either uniform corrosion or non-uniform corrosion [28-30], but these studies have not satisfied the orthogonal condition [23]. Therefore, the present study employs the phase-field method with the strain orthogonal conditions to investigate the effect of the rebar positioning and uniform versus non-uniform corrosion on concrete fracture in several typical RC cross-sections. The results obtained will provide a comprehensive overview of damage development in the realistic RC cross-sections. This will assist in the selection and rebar installation in the RC structures exposed to corrosive environments, to minimize damage caused by rebar corrosion.

To achieve the aforementioned goals, this present paper has the outlines, as follows: The methodology section describes the phase-field modeling with the orthogonal condition of the strain tensor for the uniform or the non-uniform corrosion-induced fracture. The next section presents some numerical examples corresponding to the typical RC structures. In each example, we compare the crack initiation and propagation, as well as the displacement of rust expansion under both uniform and non-uniform corrosion conditions. Finally, several conclusions are provided.

## METHODOLOGY

### *Phase-field modeling with the orthogonal condition of the strain tensor*

We use a cracked solid $V \in \mathbb{R}^{\mathcal{D}}$ (with $\mathcal{D} = 2, 3$), and $\partial V \in \mathbb{R}^{\mathcal{D}-1}$ is its external boundary. A crack surface $\Gamma$ which may propagate within the solid $V$. In a regularized representation, a scalar phase-field variable $d(\boldsymbol{x})$ is used to describe the damage state within the solid $V$ (i.e., $d(\boldsymbol{x})=0$ when the solid is completely intact, $d(\boldsymbol{x})=1$ when the solid has cracks). Regarding [18-20, 24], the energy total within the solid $V$ is determined as follows:

$$\hat{\Psi}(\boldsymbol{u},d)=\int_V \psi_u(\boldsymbol{\varepsilon},d)dV+\int_V G_c\gamma(d,\nabla d)dV \tag{1}$$

in which, the operator $\nabla d$ is the gradient of the phase-field variable $d(\boldsymbol{x})$; the function $\gamma(d,\nabla d)=\frac{d^2}{2l}+\frac{l}{2}(\nabla d\cdot\nabla d)$ denotes the crack surface density function, with $l$ is the length parameter which describes the width of the smeared crack; $G_c$ denotes the fracture toughness of the material. In the case of the brittle materials, the strain tensor $\boldsymbol{\varepsilon}$ is split into a negative part $\boldsymbol{\varepsilon}^-$ and a positive part $\boldsymbol{\varepsilon}^+$ such as $\boldsymbol{\varepsilon}=\boldsymbol{\varepsilon}^++\boldsymbol{\varepsilon}^-$. When considering the major symmetry of the tensor of the elastic stiffness $\mathbb{C}$, we have:

$$\psi(\boldsymbol{\varepsilon})=\psi(\boldsymbol{\varepsilon}^++\boldsymbol{\varepsilon}^-)=\frac{1}{2}\boldsymbol{\varepsilon}^+:\mathbb{C}:\boldsymbol{\varepsilon}^++\frac{1}{2}\boldsymbol{\varepsilon}^-:\mathbb{C}:\boldsymbol{\varepsilon}^-+\boldsymbol{\varepsilon}^+:\mathbb{C}:\boldsymbol{\varepsilon}^- \tag{2}$$

From [23], the strain energy $\psi(\boldsymbol{\varepsilon})$ is split into a positive part $\psi^+(\boldsymbol{\varepsilon}^+)$ and a negative part $\psi^-(\boldsymbol{\varepsilon}^-)$, it means $\psi(\boldsymbol{\varepsilon})=\psi^+(\boldsymbol{\varepsilon}^+)+\psi^-(\boldsymbol{\varepsilon}^-)$ with:

$$\psi^+(\boldsymbol{\varepsilon}^+)=\frac{1}{2}\boldsymbol{\varepsilon}^+:\mathbb{C}:\boldsymbol{\varepsilon}^+,\ \text{and}\ \ \psi^-(\boldsymbol{\varepsilon}^-)=\frac{1}{2}\boldsymbol{\varepsilon}^-:\mathbb{C}:\boldsymbol{\varepsilon}^- \tag{3}$$

Eqn. (3) is obtained if the two strain parts $\boldsymbol{\varepsilon}^+$ and $\boldsymbol{\varepsilon}^-$ must satisfy the following orthogonal condition in the context of the inner product with the elastic stiffness tensor $\mathbb{C}$ behaving as a metric:

$$\boldsymbol{\varepsilon}^+:\mathbb{C}:\boldsymbol{\varepsilon}^-=0 \tag{4}$$

and then, using the phase-field variable $d(\boldsymbol{x})$ to denote the damage state of material, the function of the elastic strain energy density $\psi_u$ in Eqn. (1) is defined:

$$\psi_u=\{g(d)\}\ \psi^+(\boldsymbol{\varepsilon}^+)+\psi^-(\boldsymbol{\varepsilon}^-) \tag{5}$$

in which, the function $g(d)=(1-d)^2+\kappa_d$ denotes the function of the quadratic degradation, where the dimensionless parameter $\kappa_d<<1$ helps the stability of numerical simulation after the occurrence of the structural fracture.

Then, the strain orthogonal condition of Eqn. (4) is analyzed into $(\mathbb{C}^{1/2}:\boldsymbol{\varepsilon}^+):(\mathbb{C}^{1/2}:\boldsymbol{\varepsilon}^-)=0$. We let $\hat{\boldsymbol{E}}$ being a transformed space of the strain tensor space $\boldsymbol{E}$, with $\hat{\boldsymbol{E}}=\{\hat{\boldsymbol{\varepsilon}}\,|\,\hat{\boldsymbol{\varepsilon}}=\mathbb{C}^{1/2}\boldsymbol{\varepsilon}\ \text{and}\ \boldsymbol{\varepsilon}\in\boldsymbol{E}\}$; let $\hat{\boldsymbol{\mathcal{S}}}^+$ and $\hat{\boldsymbol{\mathcal{S}}}^-$ denoting the positive and negative convex subsets, thus we have $\hat{\boldsymbol{E}}=\hat{\boldsymbol{\mathcal{S}}}^+\oplus\hat{\boldsymbol{\mathcal{S}}}^-$. Let $\hat{\boldsymbol{\varepsilon}}\in\hat{\boldsymbol{E}}$ being devided into $\hat{\boldsymbol{\varepsilon}}^+\in\hat{\boldsymbol{\mathcal{S}}}^+$ and $\hat{\boldsymbol{\varepsilon}}^-\in\hat{\boldsymbol{\mathcal{S}}}^-$, the orthogonal condition in Eqn. (4) is analyzed as $\hat{\boldsymbol{\varepsilon}}=\hat{\boldsymbol{\varepsilon}}^++\hat{\boldsymbol{\varepsilon}}^-$, and $\hat{\boldsymbol{\varepsilon}}^+:\hat{\boldsymbol{\varepsilon}}^-=0$; in which $\|\hat{\boldsymbol{\varepsilon}}-\hat{\boldsymbol{\varepsilon}}^\pm\|^2=\min_{\hat{\boldsymbol{\varsigma}}\in\hat{\boldsymbol{\mathcal{S}}}^\pm}(\hat{\boldsymbol{\varepsilon}}-\hat{\boldsymbol{\varsigma}}):(\hat{\boldsymbol{\varepsilon}}-\hat{\boldsymbol{\varsigma}})$ (see in [23-25]). Thus, the two convex subsets of $\hat{\boldsymbol{\mathcal{S}}}^\pm$ are addressed by:

$$\hat{\boldsymbol{\mathcal{S}}}^+=\{\hat{\boldsymbol{\varepsilon}}\in\hat{\boldsymbol{E}}\ |\,Tr(\hat{\boldsymbol{\varepsilon}})\geq 0\};\ \text{and}\ \hat{\boldsymbol{\mathcal{S}}}^-=\left\{\hat{\boldsymbol{\varepsilon}}\in\hat{\boldsymbol{E}}\,|\ \hat{\boldsymbol{\varepsilon}}=\frac{Tr(\hat{\boldsymbol{\varepsilon}})}{\mathcal{D}}\boldsymbol{I}\ \text{with}\ Tr(\hat{\boldsymbol{\varepsilon}})\leq 0\right\} \tag{6}$$

To satisfy the aforementioned orthogonal conditions and Eqn. (6), the two strain parts of $\hat{\boldsymbol{\varepsilon}}^\pm$ are analyzed by:

$$\hat{\boldsymbol{\varepsilon}}^{+}=\frac{1}{\mathcal{D}}\left\langle Tr\left(\hat{\boldsymbol{\varepsilon}}\right)\right\rangle_{+}\boldsymbol{I}+\hat{\boldsymbol{\varepsilon}}^{dev};\ \text{with}\quad \hat{\boldsymbol{\varepsilon}}^{-}=\frac{1}{\mathcal{D}}\left\langle Tr\left(\hat{\boldsymbol{\varepsilon}}\right)\right\rangle_{-}\boldsymbol{I} \tag{7}$$

in Eqn. (7), the deviatoric tensor $\hat{\boldsymbol{\varepsilon}}^{dev}$ is given:

$$\hat{\boldsymbol{\varepsilon}}^{dev}=\hat{\boldsymbol{\varepsilon}}-\frac{1}{\mathcal{D}}Tr\left(\hat{\boldsymbol{\varepsilon}}\right)\boldsymbol{I} \tag{8}$$

According to Refs. [24, 25], the phase-field variable $d(\boldsymbol{x})$ and displacement vector $\boldsymbol{u}(\boldsymbol{x})$ are determined by solving the staggered procedure of the following equation systems of (9) and (10):

$$\begin{cases} 2(1-d)\hat{\mathcal{H}}-\dfrac{G_c}{l}\delta_d\gamma\left(d,\nabla d\right)=0 & \text{in } V \\ d(\boldsymbol{x})=1 & \text{on } \Gamma \\ \nabla d(\boldsymbol{x})\cdot\boldsymbol{n}=0 & \text{on } \partial V \end{cases} \tag{9}$$

in which, $\delta_d\gamma\left(d,\nabla d\right)=\dfrac{d}{l}-l\Delta d$ denote the derivative of the crack surface density function $\gamma\left(d,\nabla d\right)$ with the phase-field variable $d$; the function $\hat{\mathcal{H}}=\max\limits_{\tau\in[0,t]}\left\{\psi^{+}\left(\boldsymbol{\varepsilon}^{+},\tau\right)\right\}$ of Eqns. (9) is the strain history function.

We have the following equation systems (10) to handle the displacement vector $\boldsymbol{u}(\boldsymbol{x})$:

$$\begin{cases} \nabla\cdot\boldsymbol{\sigma}-\boldsymbol{f}_{bo}=0 & \text{in } V \\ \boldsymbol{u}(\boldsymbol{x})=\hat{\boldsymbol{u}} & \text{on } \partial V_u \\ \boldsymbol{\sigma}\cdot\boldsymbol{n}=\hat{\boldsymbol{F}} & \text{on } \partial V_F \end{cases} \tag{10}$$

in Eqns. (10), the vector $\boldsymbol{n}$ denotes the normal vector of the external boundary $\partial V=\partial V_u+\partial V_F$; where $\partial V_F$ and $\partial V_u$ are the force boundary and the displacement boundary, respectively; $\boldsymbol{f}_{bo}$ is the body force in domain $V$; $\hat{\boldsymbol{F}}$ and $\hat{\boldsymbol{u}}$ denote the prescribed tension force and displacement, respectively; from Eqns. (3), (5), (7) and (8), the stress tensor $\boldsymbol{\sigma}$ is defined as $\boldsymbol{\sigma}=\dfrac{\partial\psi_u}{\partial\boldsymbol{\varepsilon}}$.

*Description of the uniform/ non-uniform corrosion in the phase-field method*

The uniform corrosion condition is illustrated in Fig. 1a, where the corrosion products cause uniform displacement $u$, which is due to the radial pressure applied at the interface between the rebar and the concrete. The increase of the rust pressure leads to concrete cracking, and the crack propagates to the edges of the cross-section. In Fig. 1a, $D$ and $D_c$ represent the diameters of the initial rebar and the corroded rebar, respectively; $d_c$ denotes the corrosion-induced loss of the rebar.

Besides, the non-uniform corrosion condition is used in this paper to adopt the semi-elliptical model of [30], as shown in Fig. 1b. In Fig. 1b, the rust expansion displacement $u(\alpha)$ is varied with angle $\alpha$, as described by the following expression (see [30]):

$$u(\alpha)=\begin{cases} \dfrac{\left(R+u_2\right)\left(R+u_2\right)}{\sqrt{\left(R+u_1\right)^2\cos^2\left(\alpha\right)+\left(R+u_2\right)^2\sin^2\left(\alpha\right)}}-R & \text{if } 0\le\alpha\le\pi \\ u_2 & \text{if } \pi\le\alpha\le 2\pi \end{cases} \tag{11}$$

in which $R$ is the radius of the initial rebar, with $D = 2R$; $u_1$ and $u_2$ represent the maximum and minimum displacements caused by the rust expansion of the rebar, where $u_2 = u_1 / 30$ (see in [30]).

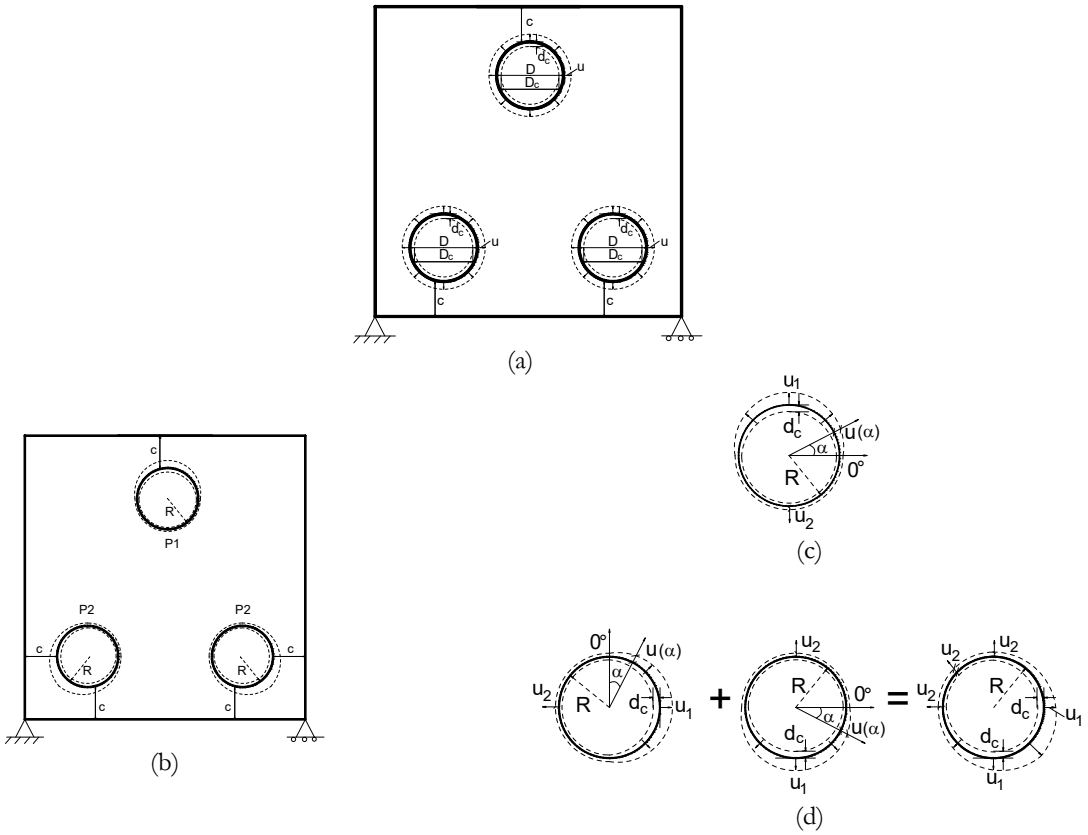


Figure 1: Description of the rebar corrosion: (a) uniform corrosion; (b) non-uniform corrosion; (c) non-uniform corrosion at the position P1 in (b); (d) non-uniform corrosion at the position P2 in (b).

Note that the rebar corrosion at the position P1 (in Figs. 1(b-c)) will differ from the rebar corrosion at the position P2 (in Figs. 1(b) and 1(d)). In this paper, the rebar at the position P2 is placed equidistant from both edges of the cross-section as depicted in Fig. 1b, so-called the concrete cover thichness c. This results in the rust expansion displacement being described as a combined effect, as illustrated in Fig. 1(d). Meanwhile, the rust expansion displacement at position the P1 is shown in Fig. 1(c).

## NUMERICAL EXAMPLES

All examples are conducted using the phase-field modeling of the strain orthogonal condition, which is described in the methodology section. The material properties are employed as in [31], in which: Elastic modulus $E$=25000 MPa; Fracture toughness $G_c$ =0.005 N/mm; Poisson's ratio $\upsilon$ =0.25; Length parameter $l$ =0.5 mm. The boundary condition and the loading condition are depicted in Figs. 1(a-b). The lower-left node is fixed in both vertical and horizontal directions. The lower-right node: the vertical displacement is fixed, while the horizontal displacement is free. Both uniform corrosion and non-uniform corrosion conditions are applied in each example. For the case of the uniform corrosion, the rust expansion displacement of each simulation step $\Delta u = 10^{-5}$ mm around the rebar is assumed to be constant during the simulation process. In the case of the non-uniform corrosion, we use the maximum expansion displacement $\Delta u_1 = 10^{-5}$ mm, the minimum expansion displacement is used as $\Delta u_2 = \Delta u_1 / 30$, and the other positions have the expansion displacement $\Delta u(\alpha)$ in polar coordinates, as depicted in Eqn. (11).

The objective of these examples is to use the phase-field method with cases of both uniform and non-uniform corrosion, as outlined in the methodology section, to investigate the crack initiation and propagation, as well as the rust expansion displacement at the time of the crack initiation (so-called the time $t_1$) and at the time when the crack propagates to the edge of the structure (so-called the time $t_2$) in the following problems: (i) The arrangement of one rebar or numerous rebars such that the area total of the rebars is equivalent, and the concrete cover thickness is fixed c=15mm. In this regard, the paper simulates the damage of the cross-sections containing various numbers and diameters of the rebars, which are asymmetrically arranged, as detailed in Tab. 1 and Figs. 2(a-d), respectively; (ii) The investigation of the arrangement of four D10 rebars symmetrically positioned at the four corners of the cross-section (denoted the 4-D10-T2 type) and the four edges of the cross-section (denoted the 4-D10-T3 type), with the concrete cover thicknesses c=10mm, 15mm, and 20mm, as shown in Fig. 2(e) and Fig. 2(f), respectively; (iii) The simulation of the damage in the type of 4-D10-T3 containing the periodically distributed pores with the pore diameter of 8mm and the concrete cover thickness c=20mm (as shown in Fig. 2(g)). The RC cross-sections have the dimensions L×H=100×100mm, and the boundary conditions are as described in Figs. 1(a-b).

| Samples | One D20 rebar | Two D14 rebars | Three D12 rebars | Four D10 rebars |
|---|---|---|---|---|
| Label | 1-D10 | 2-D14 | 3-D12 | 4-D10 |
| Total area (mm²) | 314 | 308 | 339 | 314 |

Table 1: Cross-section containing one rebar or numerous rebars with the equivalent rebar area fractions.

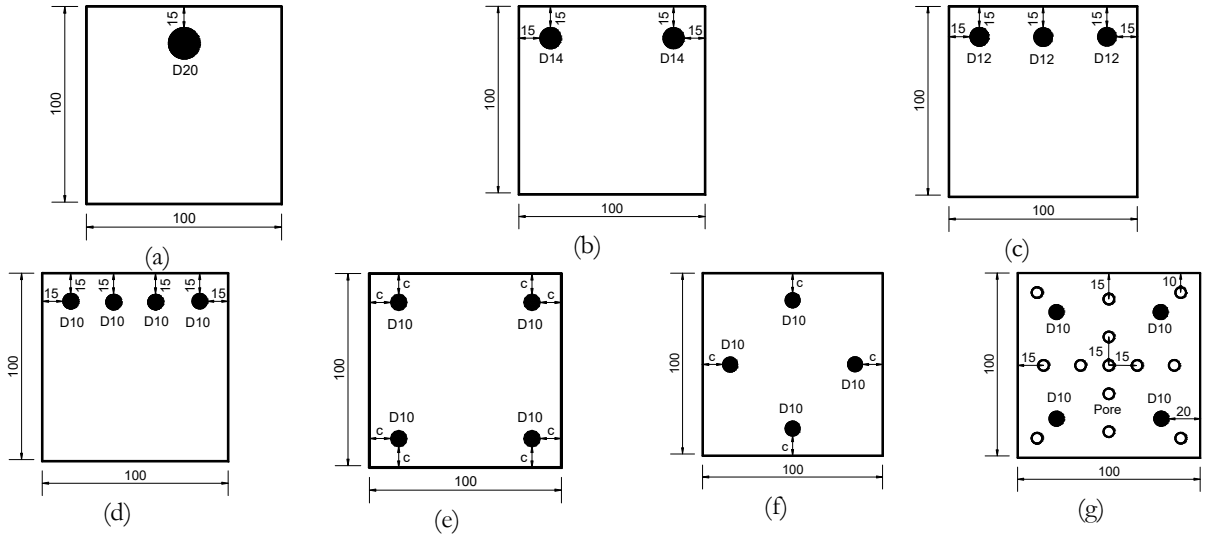


Figure 2: Dimensions of the cross-section containing the rebars: (a) 1-D20; (b) 2-D14; (c) 3-D12; (d) 4-D10-T1; ((a)-(d) concrete cover thickness c=15mm); (e) Type of 4-D10-T2 with c=10mm, 15mm, and 20mm; (f) Type of 4-D10-T3 with different values of c=10mm, 15mm, and 20mm; (g) Type of 4-D10-T2 containing the pores with c=20mm (so-called 4-D10-T2-P-C20).

*Investigation of the corrosion-induced damage with equivalent fractions of the rebar area*

The proposed phase-field method of the strain orthogonal conditions can be validated by comparing the complete crack path between the simulation result and the result of the realistic accelerated corrosion experiments from our project, using two D14 rebars and the concrete cover thickness of c=15mm, as shown in Fig. 3. It is observed that the crack paths between the two aforementioned methods are very similar. Therefore, this proposed simulation method can be applied to the next examples to achieve the objectives of this paper.

Figs. 4-9 compare the initiation and development of the cracks in the samples containing one rebar or numerous asymmetrically arranged rebars. The fixed concrete cover thickness is c=15mm. Fig. 4 shows that, for the uniform corrosion condition, the crack propagates directly to the edge of the cross-section (see Figs. 4(a-b)). Regarding this problem, the rust expansion displacements from the times $t_1$ and $t_2$ are very small (see Fig. 10). In the case of non-uniform corrosion, in addition to the crack propagating to the edge of the cross-section, two other branches of the crack

developing along the edges of the cross-section (see Figs. 4(c-d)). Thus the rust expansion displacements at these two times $t_1$ and $t_2$ are larger compared to the uniform corrosion case (see Fig. 10).

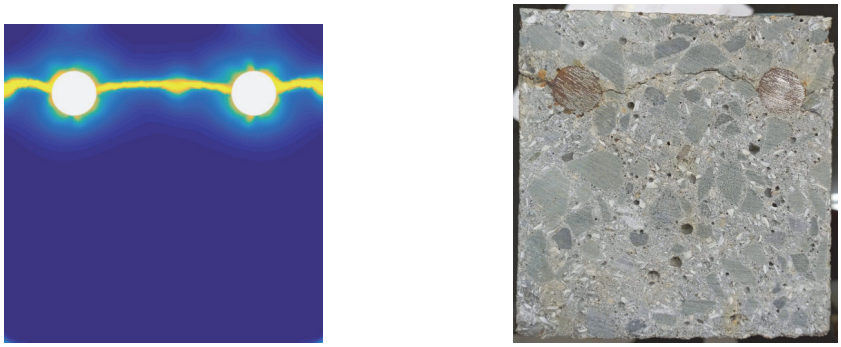

(a) (b)

Figure 3: Comparison of the crack development on the 2-D14 cross-section between simulation method (a) and experiment (b).

(a) (b) (c) (d)

Figure 4: Crack development on the 1-D20 cross-section and c=15mm: (a) crack nucleation and (b) complete crack development due to the uniform corrosion; (c) crack nucleation and (d) complete crack development due to the non-uniform corrosion.

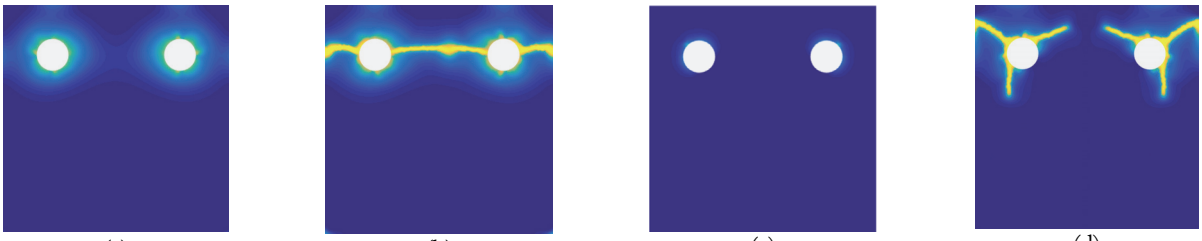

(a) (b) (c) (d)

Figure 5: Crack development on the 2-D14 cross-section and c=15mm: (a) crack nucleation and (b) complete crack development due to the uniform corrosion; (c) crack nucleation and (d) complete crack development due to the non-uniform corrosion.

Fig. 5 compares the nucleation and the propagation of the cracks on the RC cross-section of the 2-D14 type under the two corrosion conditions. In Fig. 5(b), for uniform corrosion, the crack propagates from the rebars and spreads horizontally toward the edge of the structure. Unlike Fig. 5(b), in Fig. 5(d), for non-uniform corrosion, the crack propagates toward the edge with a tendency to incline towards the corner of the structure, because in this zone of the structure, the rebars are subjected to the most severe corrosion, which corresponds with the position P2 (see Fig. 1(b) and Fig. 1(d)). Additionally, other cracks develop parallel to the other edges of the RC cross-section.

Figs. 6-7 illustrate the corrosion-induced damage for the 3-D12 and the 4-D10-T1 cross-sections, in which the rebars are arranged into a single row and evenly spaced (see in Figs. 2(c-d). It is observed that for these two types of structures, the crack initiation and propagation trends are similar. However, the differences of the crack patterns emerge between the two corrosion conditions. For the uniform corrosion, the crack propagates horizontally from the rebars toward the edge of the structures (see Figs. 6(b) and 7(b)). In the case of the non-uniform corrosion, the cracks propagate to the edges of the structure, directed toward the corner of the cross-section. Additionally, other crack branches develop parallel to the two vertical edges of the structures (see Figs. 6(d) and 7(d)).

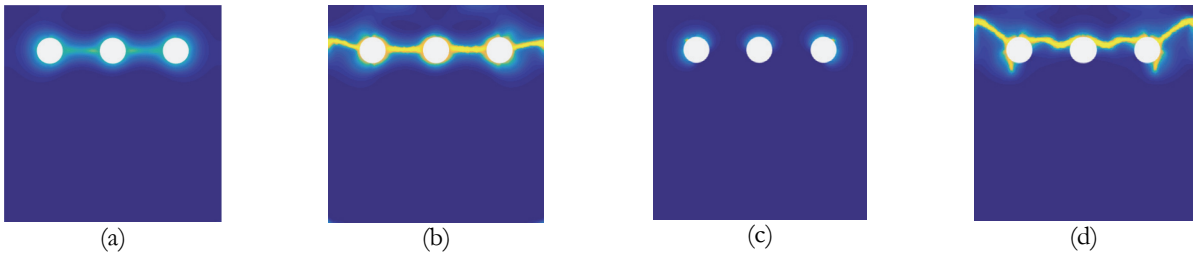

(a) (b) (c) (d)

Figure 6: Crack development on the 3-D12 cross-section and c=15mm: (a) crack nucleation and (b) complete crack development due to the uniform corrosion; (c) crack nucleation and (d) complete crack development due to the non-uniform corrosion.

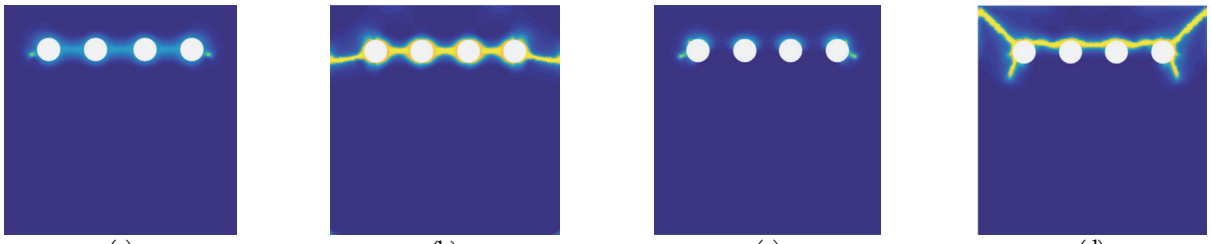

(a) (b) (c) (d)

Figure 7: Crack development on the 4-D10-T1 cross-section and c=15mm: (a) crack nucleation and (b) complete crack development due to the uniform corrosion; (c) crack nucleation and (d) complete crack development due to the non-uniform corrosion.

From Fig. 10, it is observed that for the three structural types of the 2-D14, 3-D12, and 4-D10-T1, the rust expansion displacement distances between the two times $t_1$ and $t_2$ of the uniform corrosion condition are smaller than the results of the non-uniform corrosion condition. The the rust expansion displacement values at the time $t_1$ of the non-uniform corrosion are smaller than ones of the uniform corrosion. In contrast, the rust expansion values at the time $t_2$ of the non-uniform corrosion are larger than ones of the uniform corrosion. When considering both uniform and non-uniform corrosion conditions, the rust expansion displacement values at the two times $t_1$ and $t_2$ decrease progressively across the 2-D14, 3-D12, and 4-D10-T1 structures. For the 2-D14 structure, the rust expansion displacement distance between the two times $t_1$ and $t_2$ is very small. It can be inferred that after corrosion begins, the larger the diameter of the rebar, the greater the volume of rust products generated, which leads to faster crack propagation.

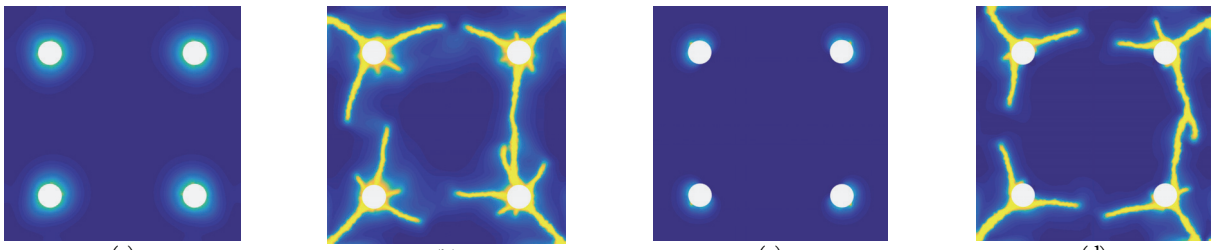

(a) (b) (c) (d)

Figure 8: Crack development on the 4-D10-T2 cross-section and c=15mm: (a) crack nucleation and (b) complete crack development due to the uniform corrosion; (c) crack nucleation and (d) complete crack development due to the non-uniform corrosion.

Fig. 1(e) describes the RC cross-section containing four D10 rebars, which are arranged symmetrically at the four corners of the structure (denoted the 4-D10-T2 type). From Fig. 8, it can be seen that, for this rebar arrangement, the crack development is similar under both uniform and non-uniform corrosion conditions. Specifically, the four cracks propagate towards the four corners of the cross-section, while the other cracks tend to develop parallel to the edges of the cross-section, causing the entire concrete cover layer to detach from the rebars (see Figs. 8(b) and 8(d)).
Fig. 1(f) depicts the symmetric arrangement of the four D10 rebars at the four edges of the cross-section, (denoted the 4-D10-T3 type). From Fig. 9, for this rebar configuration, the clear difference is observed in the crack development between the uniform corrosion and the non-uniform corrosion conditions. For the uniform corrosion, it can be seen that the cracks develop in the diamond-shaped pattern, meaning that, in addition to cracks propagating directly to the edges of the cross-section, the remaining cracks connect to each other along the shortest distances between the rebars (see Fig. 9(b)).

In contrast, under the non-uniform corrosion condition, the main cracks propagate parallel to the edges of the cross-section, leading to the delamination of the concrete cover layer (see Fig. 9(d)).

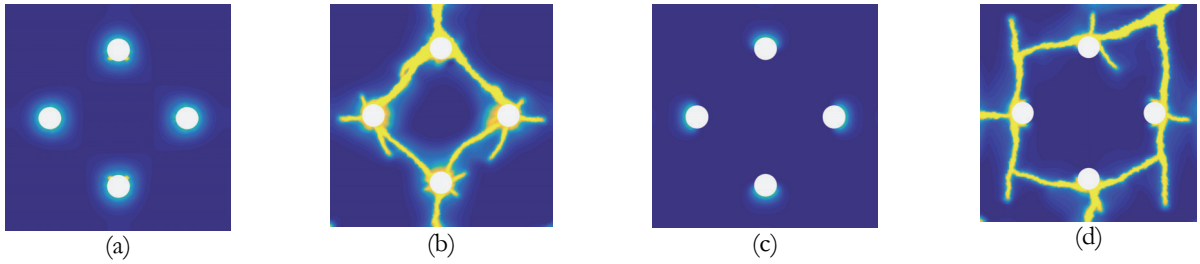


Figure 9: Crack development on the 4-D10-T3 cross-section and c=15mm: (a) crack nucleation and (b) complete crack development due to the uniform corrosion; (c) crack nucleation and (d) complete crack development due to the non-uniform corrosion.

From Fig. 10, for the 4-D10-T2 and the 4-D10-T3 types, the rust expansion displacement at the time $t_1$ under the non-uniform corrosion condition is smaller than the corresponding value under the uniform corrosion condition. In contrast, the rust expansion displacement at the time $t_2$ under the non-uniform corrosion condition is significantly larger than the displacement under the uniform corrosion condition.

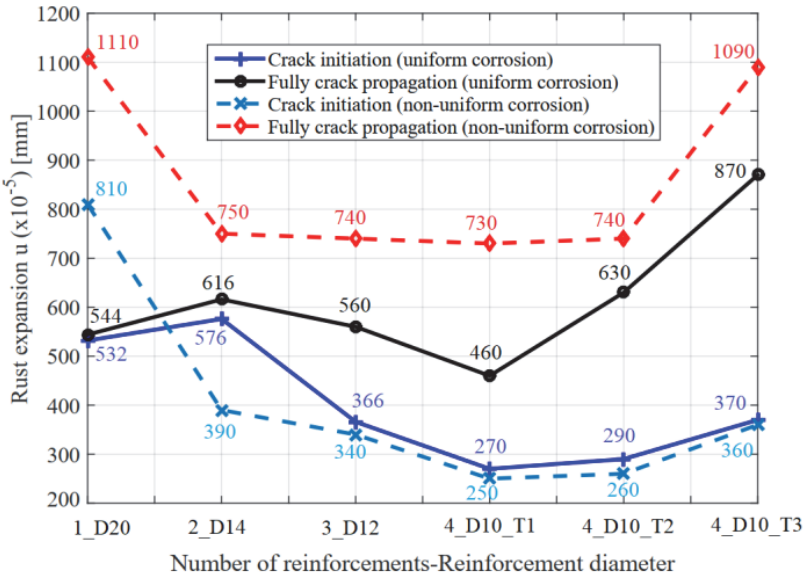


Figure 10: Comparisons of total displacement of the rust expansion between the cross-section containing rebars: 1-D20 ; 2-D14 ; 3-D12 ; 4-D10-T1 ; 4-D10-T2; 4-D10-T3 with the concrete cover thickness c=15mm.

The following observations are also provided in Fig. 10: (i) For each structural configuration with the different rebar arrangements, the rust expansion displacement values at the time $t_1$ under the uniform corrosion condition are always greater than those under the non-uniform corrosion condition. In contrast, the rust expansion displacement values at the time $t_2$ under the uniform corrosion are always smaller than those under the non-uniform corrosion, except for the 1-D20 configuration; (ii) For the 1-D20 and the 2-D14 configurations, under the condition of the uniform corrosion, the difference between the rust expansion displacement values at the times $t_1$ and $t_2$ is very small, meaning the crack propagates very quickly to the edges of the cross-section after the crack initiation; (iii) For the four D10 rebars, the rust expansion displacement values at the times $t_1$ and $t_2$ are increase progressively with the 4-D10-T1, 4-D10-T2, and 4-D10-T3 configurations for both two corrosion conditions.

*Investigation of the corrosion-induced damage with the rebar layout and the concrete cover thickness changed*

This section investigates the damage in the cross-sections containing the four D10 rebars arranged at the four corners (denoted the 4-D10-T2 type in Fig. 2(e)) and the four rebars arranged along the four edges (denoted the 4-D10-T3 type in Fig. 2(f)), with varying concrete cover thicknesses.

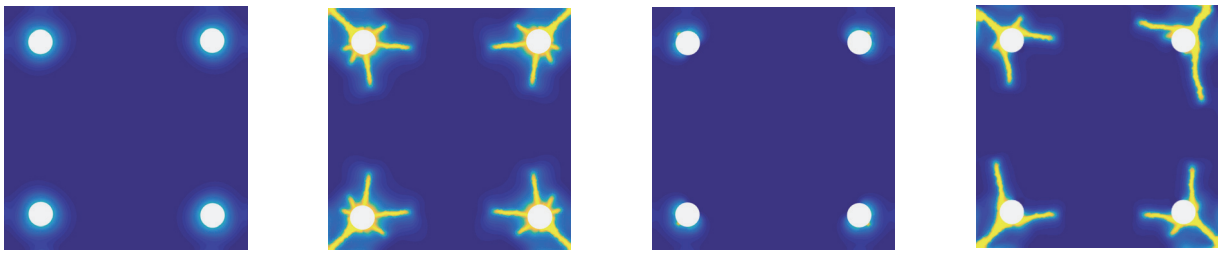

(a) (b) (c) (d)

Figure 11: Crack development on the 4-D10-T2 cross-section and c=10mm: (a) crack nucleation and (b) complete crack development due to the uniform corrosion; (c) crack nucleation and (d) complete crack development due to the non-uniform corrosion.

Fig. 11 illustrates the crack propagation paths under the conditions of the uniform and the non-uniform corrosion for the 4-D10-T2 type with the concrete cover thickness c=10mm. The primary crack paths between these two corrosion conditions include the cracks propagating toward the corner of the cross-section and other cracks extending parallel to the edges of the cross-sections (see Fig. 11(b) and Fig. 11(d)). Fig. 16 compares the rust expansion displacement values at the times $t_1$ and $t_2$ for these structures under the two corrosion conditions. It is observed that the rust expansion displacement values are quite similar at the times $t_1$ and $t_2$, which can be explained by the thin concrete cover thickness, this phenomenon leads to the similar crack propagation paths.

Fig. 12 provides the crack propagation under the conditions of the uniform and the non-uniform corrosion for the 4-D10-T3 type with the concrete cover thickness c=10mm. Figs. 12(a-b) describe the damage due to the uniform corrosion condition. The crack propagation direction is generally similar to that observed for the 4-D10-T3 type with the concrete cover thickness c=15mm (see Fig. 9(b)). In this case, the main crack paths include: the cracks propagate toward the edge of the cross-section, and the secondary cracks develop in the diamond pattern between the shortest distances of the rebars (see Fig. 12(b)). In contrast, under the non-uniform corrosion condition, the primary crack propagation direction is parallel to the edges of the cross-section, leading to the delamination of the concrete cover layer from the cross-section (as shown in Fig. 12(d)).

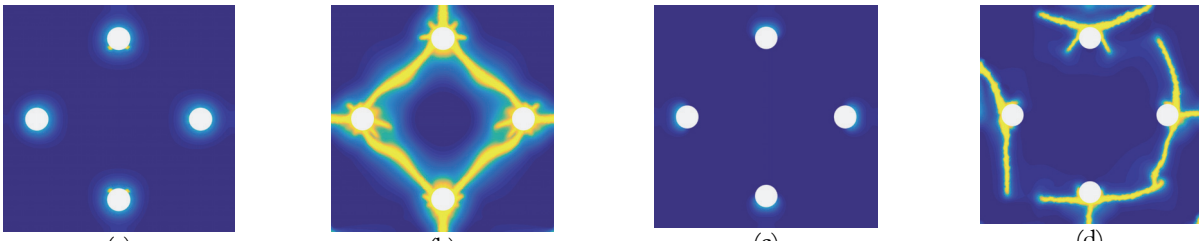

(a) (b) (c) (d)

Figure 12: Crack development on the 4-D10-T3 cross-section and c=10mm: (a) crack nucleation and (b) complete crack development due to the uniform corrosion; (c) crack nucleation and (d) complete crack development due to the non-uniform corrosion.

Fig. 16 shows that, at the time $t_1$, for the 4-D10-T3 type with the concrete cover thickness of c=10 mm, the rust expansion displacements under the two corrosion conditions are nearly identical and also similar to the rust expansion displacement at the time $t_1$ for the 4-D10-T2 type. However, at the time $t_2$, the rust expansion displacement value for the non-uniform corrosion condition is significantly larger than that for the uniform corrosion condition, due to the distinctly different crack propagation trends between the two corrosion conditions.

Fig. 13 compares the initiation and the development of the cracks in the 4-D10-T2 type with c=20 mm under the two corrosion conditions. Similar to the crack propagation trends observed for this type of the cross-sections with c=10 mm (see Fig. 11) and c=15 mm (see Fig. 8), for the concrete cover thickness of c= 20 mm, the two main types of the crack remain as follows: the cracks propagate toward the corner of the cross-sections, and the secondary cracks develop parallel to the edges of the cross-sections, leading to delamination of the concrete cover layer. The damage progression trends under both corrosion conditions are quite similar, resulting in similar rust expansion displacement values at the times $t_1$ and $t_2$ between both corrosion conditions (see Fig. 16).

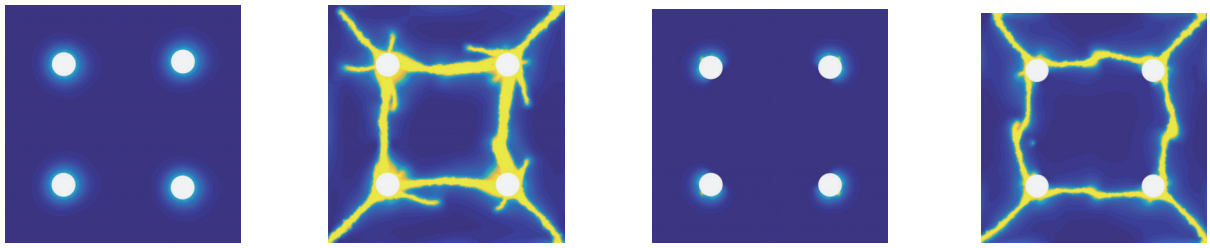

(a) (b) (c) (d)

Figure 13: Crack development on the 4-D10-T2 cross-section and c=20mm: (a) crack nucleation and (b) complete crack development due to the uniform corrosion; (c) crack nucleation and (d) complete crack development due to the non-uniform corrosion.

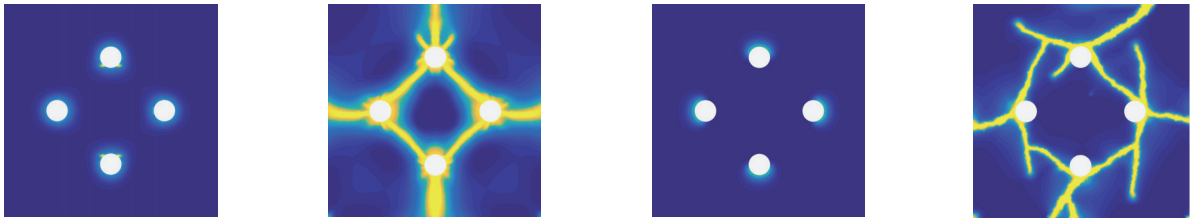

(a) (b) (c) (d)

Figure 14: Crack development on the 4-D10-T3 cross-section and c=20mm: (a) crack nucleation and (b) complete crack development due to the uniform corrosion; (c) crack nucleation and (d) complete crack development due to the non-uniform corrosion.

Fig. 14 predicts the damage for the 4-D10-T3 type with c=20mm. For the uniform corrosion condition, the crack propagation trend of this case is similar to that observed for the 4-D10-T3 type with c= 10mm and 15mm. The two distinct types of characteristic cracks as follows: the cracks propagate straight toward the edges of the structures and the cracks have the diamond shape (see Figs. 9(b), 12(b), and 14(b)).

The non-uniform corrosion condition, as presented in Fig. 14(d), results in complex crack propagation due to the large concrete cover thickness. However, the crack propagation pattern can still be observed, revealing the following trends: The first type of crack tends to develop perpendicular to the edge of the cross-section from the rebars, while the second crack path arises from the competition between the cracks which are parallel to the edges of the structure and the cracks which take on the diamond shape of the uniform corrosion (see Fig. 14(d)). The second crack type exists because the distance between the adjacent rebars is relatively small, and the corrosion-induced expansion between these two adjacent rebars affects each other. Fig. 16 demonstrates that, at the time $t_1$, for the 4-D10-T3 type with c= 20 mm, the rust expansion displacements for both conditions are nearly the same and closely resemble those observed at the time $t_1$ for the 4-D10-T2 type. However, for this structural type, at the time $t_2$, the rust expansion displacement value for the non-uniform corrosion condition is significantly greater than that for the uniform corrosion condition, due to the distinct differences in the crack propagation trends between the two corrosion conditions.

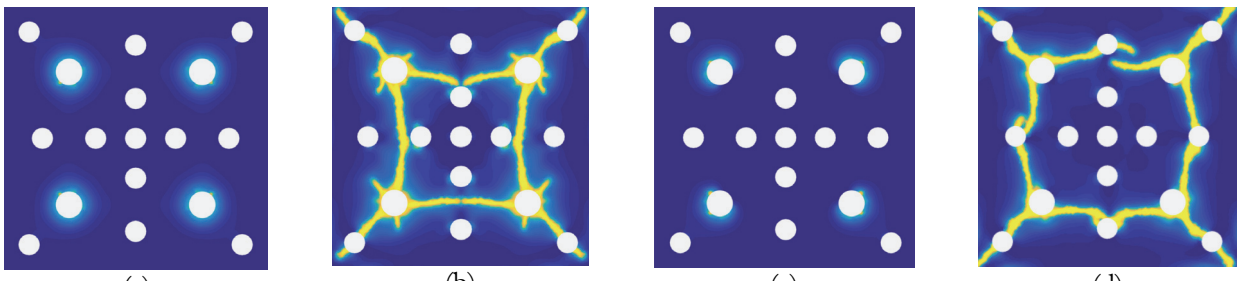

(a) (b) (c) (d)

Figure 15: Crack development on 4-D10-T2 cross-section containing pores and c=20mm (denoted type 4-D10-T2-P-C20): (a) crack nucleation and (b) complete crack development due to the uniform corrosion; (c) crack nucleation and (d) complete crack development due to the non-uniform corrosion.

This final example predicts the damage of the 4-D10-T2 type with c= 20 mm, containing 13 uniformly distributed circular pores with their diameter of 8 mm (denoted the 4-D10-T2-P-C20 type), as presented in Fig. 2(g). The aim of this example

is to investigate the effect of the pores on the crack nucleation and propagation, as well as on the rust expansion displacements, under both the uniform and the non-uniform corrosion conditions.

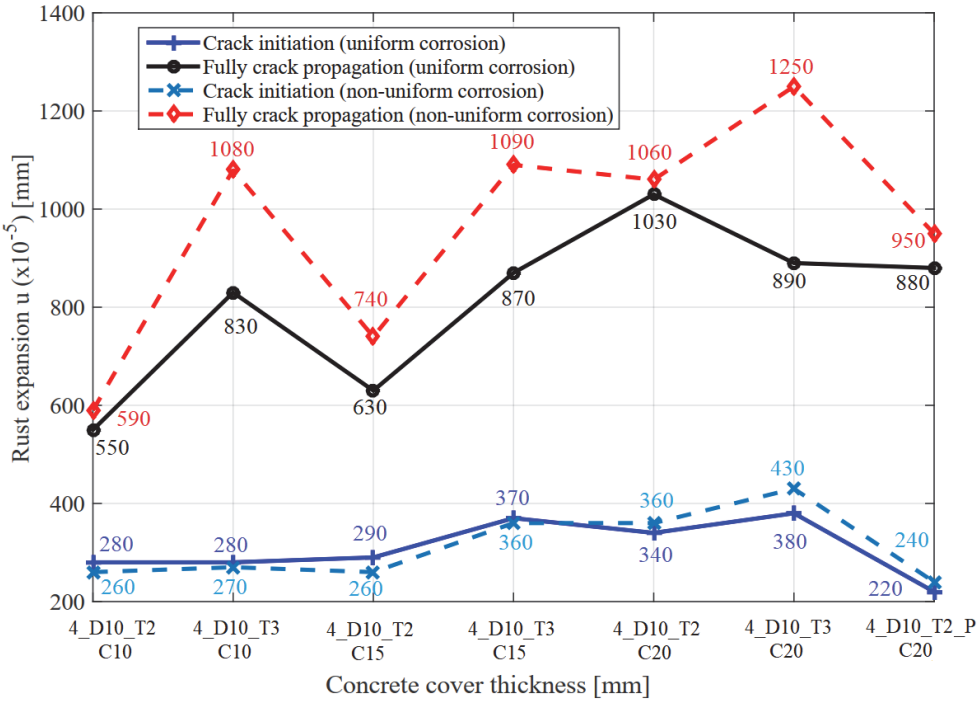


Figure 16: Comparisons of total displacement of the rust expansion between the cross-sections of 4-D10-T2 and 4-D10-T3 with c=10 mm, c=15 mm and c=20 mm.

Fig. 15 compares the damage between the two corrosion conditions. It is observed that, for the 4-D10-T2 type, with varying concrete cover thickness values and the presence or absence of the pores, the crack development is quite similar between the uniform and the non-uniform corrosion conditions. Specifically, the first crack type develops to the corner of the cross-sections, and the second crack type propagates parallel to the edges of the cross-sections. Therefore, the rust expansion displacement difference between the two corrosion conditions at the corresponding times $t_1$ and $t_2$ is not significant (see Fig. 16). However, when compared to the 4-D10-T2 structure without the pores and with c=20 mm, the rust expansion displacement values at the two times $t_1$ and $t_2$ are greater for the 4-D10-T2-P-C20 type, as shown in Fig. 16. This difference can be attributed to the higher overall stiffness of the structure without the pores compared to the structure with the pores.

From Fig. 16, it can be observed that for the 4-D10-T2 type and the 4-D10-T3 type, as well as for each corresponding corrosion condition, when the concrete cover thickness increases, the rust expansion displacement values at the two times $t_1$ and $t_2$ also increase. This indicates that structures with a larger concrete cover thickness are less affected by corrosion conditions.

## CONCLUSIONS

This paper employs the phase-field modeling with the strain orthogonal condition for the damage caused by the uniform corrosion or the non-uniform corrosion to investigate the crack initiation and propagation, as well as the rust expansion displacements at the two times $t_1$ and $t_2$ in the typical RC cross-sections. The obtained numerical results lead to the following conclusions:

- In the case of one bar or multiple rebars asymmetrically arranged such that the equivalent area fractions of the rebars, with c=15mm, the damage under the uniform corrosion condition results in a single continuous crack that propagates to the edge of the cross-section. In contrast, for the non-uniform corrosion condition, in addition to the crack propagating to the edge of the cross-section, the other crack branches develop parallel to the edges of the structure.

This leads to the larger rust expansion displacement value at the time $t_2$ for the non-uniform corrosion condition compared to the corresponding values of the uniform corrosion.

- For the 1-D20 and 2-D14 configurations under the uniform corrosion condition, the crack propagates rapidly to the edge of the structures after the first crack appears.
- When c=15mm, the rust expansion displacement values at the times $t_1$ and $t_2$ increase progressively for the structural types 4-D10-T1, 4-D10-T2, and 4-D10-T3. This phenomenon can similarly be observed when the value of the concrete cover thickness c is changed.
- For both the uniform and the non-uniform corrosion conditions, and for the 4-D10-T2 type, when the concrete cover thickness changed, the crack pattern always follows this sequence: the first crack type develops from the rebar to the corner of the structure, and the second crack type propagates parallel to the edges of the structure, leading to the complete delamination of the concrete cover at all four edges. Since the crack paths are relatively similar between the two corrosion conditions, the rust expansion displacement values at the times $t_1$ and $t_2$ are also relatively similar.
- For the 4-D10-T2-C20 type with the pores, the crack propagation trend is similar to that of the structure without pores, meaning there are the cracks those develop to the corner of the structure and the other cracks propagate parallel to the structural edges under both corrosion conditions. However, the corresponding rust expansion displacement values of the structure with the pores at the times $t_1$ and $t_2$ are smaller than those of the structure without the pores. This may be due to the overall stiffness of the structure with the pores being weaker than that of the structure without the pores.
- For both the uniform and the non-uniform corrosion conditions of the 4-D10-T3 type with varying concrete cover thicknesses, the crack patterns between the two corrosion conditions differ significantly. Specifically, for uniform corrosion condition, the two main crack types exist, as follows: the first crack type propagates straight to the edges of the structure, while the second crack type develops in the diamond shape along the shortest distances between the two adjacent rebars. In contrast, for the non-uniform corrosion, the main crack propagation direction is parallel to the edges of the structure. Except for the case when c = 20mm, where the rebars are very close to each other, the damage occurs in the competition between the cracks propagating parallel to the structural edges and those in the diamond shape. Due to the more complex crack propagation path under the non-uniform corrosion condition, the rust expansion displacement value at the time $t_2$ is much greater compared to that under the uniform corrosion condition.
- In all cases of varying concrete cover thicknesses and for the 4-D10-T2 type and 4-D10-T3 type, the increase of the concrete cover thickness values leads to a corresponding increase in the rust expansion displacement values at both times $t_1$ and $t_2$. This indicates that a larger concrete cover thickness results in the RC structure being less affected by the corrosion conditions.

The above conclusions provide designers with an overall understanding of the damage caused by both uniform and non-uniform corrosion conditions, considering the position and the diameter of the rebars within the RC cross-sections. This insight is valuable for the appropriate arrangement of the rebars in the RC structures, helping to minimize the damage and enhance the durability of the RC structures under the corrosion conditions. In future study, we plan to extend the present work in the accelerated corrosion test on the aforementioned typical RC cross-sections, under the condition with or without stirrup reinforcements.

## ACKNOWLEDGEMENTS

This research is funded by University of Transport and Communications (UTC) under grant number T2025-CT-017.

## CONFLICTS OF INTEREST

The authors declare that they have no conflicts of interest to report regarding the present study.

## REFERENCES


[1] Lu, C., Jin, W., and Liu, R., (2011). Reinforcement corrosion-induced cover cracking and its time prediction for reinforced concrete structures. Corrosion Science, 53 (4), pp. 1337–1347.

[2] Jamali, A., Angst, U., Adey, B., and Elsener, B. (2013). Modeling of corrosion-induced concrete cover cracking: a critical analysis. Construction and Building Materials, 42, pp. 225–237.

[3] Sauman, Z., (1971). Carbonization of porous concrete and its main binding components. Cement and Concrete Research, 1 (6), pp. 645–662.

[4] Alonso, C., Andrade, C., Rodriguez, J., and Diez, J.M., (1998). Factors controlling cracking of concrete affected by reinforcement corrosion. Materials and structures, 31 (7), pp. 435–441.

[5] El Maaddawy, T.A., and Soudki, K. A., (2003). Effectiveness of impressed current technique to simulate corrosion of steel reinforcement in concrete. Journal of materials in civil engineering, 15 (1), pp. 41-47.

[6] Tran, T.T., Tran, T.M., Nguyen, X.T., Nguyen, D.H., Vu, B.T., and Vo, V.N., (2022). Influences of pre-bending load and corrosion degree of reinforcement on the loading capacity of concrete beams. Journal of the Mechanical Behavior of Materials, 31, pp. 554–563.

[7] Qiao, D., Nakamura, H., Yamamoto, Y., and Miura, T., (2016). Crack patterns of concrete with a single rebar subjected to non-uniform and localized corrosion. Construction and Building Materials, 116, pp. 366–377.

[8] Andrade, C., Molina, F.J., and Alonso, C., (1993). Cover cracking as a function of rebar corrosion: part 1-experiment test. Materials and structures, 26, pp. 453–454.

[9] Hoang, T.T.L., and Lai, T. H., (2021). Characteristics and corrosion protection of polypyrrole doped with salicylate anions on CT3 steel passivated by molydate. Transport and Communications Science Journal, 72 (7), pp. 789-799.

[10] Bhargava, K., Ghosh, A.K., Mori, Y., and Ramanujam, S., (2005). Modeling of time to corrosion induced cover cracking in reinforced concrete structures, Cement and Concrete Research, 35 (11), pp. 2203–2218.

[11] Chen, J., Zhang, W., Tang, Z., and Huang, Q., (2020). Experimental and numerical investigation of chloride-induced reinforcement corrosion and mortar cover cracking. Cement and Concrete Composites, 111, 103620.

[12] Tran, K.K., Nakamura, H., Kawamura, K., and Kunieda, M., (2011). Analysis of crack propagation due to rebar corrosion using RBSM. Cement and Concrete Composites, 33, pp. 906–917.

[13] Pan, T., Lu, Y., (2012). Stochastic modeling of reinforced concrete cracking due to nonuniform corrosion: FEM-based cross-scale analysis. Journal of Materials in Civil Engineering, 24, pp. 698–706.

[14] Yang, S.T., Li, K.F., Li, C.Q., (2018). Analytical model for non-uniform corrosion-induced concrete cracking. Magazine of Concrete Research, 90, pp. 1–10.

[15] Savija, B., Lukovic, M., Pacheco, J., Schlangen, E., (2013). Cracking of the concrete cover due to reinforcement corrosion: a two-dimensional lattice model study. Construction and Building Materials. 44, pp. 626–638.

[16] Zhang, J., Ling, X., Guan, Z., (2017). Finite element modeling of concrete cover crack propagation due to non-uniform corrosion of reinforcement. Construction and Building Materials. 132, pp. 487–499.

[17] Du, X., Jin, L., Zhang, R., (2014). Modeling the cracking of cover concrete due to non-uniform corrosion of reinforcement. Corrosion Science. 89, pp. 189–202.

[18] Francfort, G. A., and Marigo, J. J., (1998). Revisiting brittle fracture as an energy minimization problem. Journal of the Mechanics and Physics of Solids, 46 (8), pp. 1319-1342.

[19] Nguyen, T. T., Yvonnet, J., Zhu, Q. Z., Bornert, M., Chateau, C., (2015), A phase field method to simulate crack nucleation and propagation in strongly heterogeneous materials from direct imaging of their microstructure. Engineering Fracture Mechanics. 139, pp. 18–39.

[20] Nguyen, T. T., Yvonnet, J., Bornert, M., Chateau, C., Sab, K., Romani, R., Le Roy, R., (2016). On the choice of parameters in the phase field method for simulating crack initiation with experimental validation. International Journal of Fracture. 197 (2), pp. 213–226.

[21] Alessi, R., Marigo, J. J., and Vidoli, S., (2015). Gradient damage models coupled with plasticity: Variational formulation and main properties. Mechanics of Materials, 80, pp. 351-367.

[22] Hofacker, M., and Miehe, C., (2012). Continuum phase field modeling of dynamic fracture: Variational principles and staggered FE implementation. International Journal of Fracture, 178, pp. 113-129.

[23] He, Q. C., and Shao, Q., (2019). Closed-form coordinate-free decompositions of the twodimensional strain and stress for modeling tension–compression dissymmetry. Journal of Applied Mechanics, 86 (3), 031007.

[24] Vu, B.T., Le-Quang, H., and He, Q.C., (2024). A phase field method of crack nucleation investigation for experimental validation by using the improved degradation functions and strain orthogonal decompositions. Applications in Engineering Science, 17, 100173.

[25] Vu, B.T., Bui, T.T, Nguyen, N.L., Tran, T.T., Nguyen, X.L., and Hoang, V.H., (2024). Phase-field modelings of fracture investigate the influence of interfacial effects on damage and optimal material distribution in brittle inclusion-matrix structures, Forces in Mechanics, 16, 100282.

[26] Vu, B.T., Nguyen, X.L. and Do, A.T., (2023). Strain orthogonal decomposition implemented within the phase-field method with interfacial damage to model fracture in multiphase heterogeneous materials. Transport and Communications Science Journal, 74 4), pp. 386-399.

[27] Vu, B.T. (2023). Phase field modelling combined with optimization algorithm for maximizing the resistance in two-phase composites. Transport and Communications Science Journal, 74 (4), pp. 427-443.

[28] Fang, X., Pan, Z., and Ma, R., (2023). A multi-phase-field framework for non-uniform corrosion and corrosion-induced concrete cracking. Computer Methods in Applied Mechanics and Engineering, 414, pp. 116196.

[29] Fang, X., Pan, Z., and Chen, A., (2020). Phase field modeling of concrete cracking for non-uniform corrosion of rebar. Theoretical and Applied Fracture Mechanics, 121, 103517.

[30] Korec, E., Jirasek, M., Wong, H.S., Martinez-Peneda, E., (2024). Phase-field chemo-mechanical modelling of corrosion-induced cracking in reinforced concrete subjected to non-uniform chloride-induced corrosion. Theoretical and Applied Fracture Mechanics, 129, 104233.

[31] Liu, G., Li, Q., and Zuo, Z., (2016). Implementation of a staggered algorithm for a phase field model in ABAQUS, Chinese Journal of Rock Mechanics and Engineering, 35 (5), pp. 1019–1030.